journal of the mechanical behavior of biomedical materials 115 (2021) 104275

Contents lists available at ScienceDirect

Journal of the Mechanical Behavior of Biomedical Materials

journal homepage: www.elsevier.com/locate/jmbbm

Research paper

Location- and layer-dependent biomechanical and microstructural characterisation of the porcine urinary bladder wall

Robin Trostorf [a], Enrique Morales-Orcajo [a], Tobias Siebert [b], Markus Böl [a,*]

[a] Institute of Mechanics and Adaptronics, Technische Universität Braunschweig, Braunschweig D-38106, Germany
[b] Institute of Sport and Motion Science, University of Stuttgart, Stuttgart D-70569, Germany

ARTICLE INFO

Keywords:
Biaxial tension testing
Layer-specific experiments
Microstructure
Smooth muscle
Tissue staining

ABSTRACT

The knowledge of the mechanical properties of the urinary bladder wall helps to explain its storage and micturition functions in health and disease studies; however, these properties largely remain unknown, especially with regard to its layer-specific characteristics and microstructure. Consequently, this study entails the assessment of the layer-specific differences in the mechanical properties and microstructure of the bladder wall, especially during loading. Accordingly, ninety-two (n = 92) samples of porcine urinary bladder walls were mechanically and histologically analysed. Generally, the bladder wall and different tissue layers exhibit a non-linear stress–stretch relationship. In this study, the load transfer mechanisms were not only associated with the wavy structure of muscular and mucosal layers, but also with the entire bladder wall microstructure. Contextually, an interplay between the mucosal and muscular layers could be identified. Therefore, depending on the region and direction, the mucosal layer exhibited a stiffer mechanical response to equi-biaxial loading than that offered by the muscular layer when deformed to stretch levels higher than λ = 1.6 to λ = 2.2. For smaller stretches, the mucosal layer evinces no significant mechanical reaction, while the muscular layer bears the load. Owing to the orientation of its muscle fibres, the muscular layer shows an increased degree of anisotropy compared to the mucosal layer. Furthermore, the general incompressibility assumption is analysed for different layers by measuring the change in thickness during loading, which indicated a small volume loss.

1. Introduction

The bladder's functions include temporarily storing of urine at a low-pressure level (passive phase), and control of micturition (active phase). Thus, the urinary bladder (UB) is subject to enormous deformations. According to Vaughan and Satchell (1995), during the passive phase, the internal pressure is nearly constant until maximum capacity is reached. Remarkably, after micturition, the shape of the UB completely returns to its reference state. This feature requires special micromechanical load transfer mechanisms, and thus there exists a special microstructure of the urinary bladder wall (UBW), consisting of several layers (from the inside out), namely: Mucosal, muscular, and serosal layers. For more details, see Section 2.1.

To better understand aforementioned load transfer mechanisms inside the UBW, mechanical experiments in combination with detailed microstructural information on its main constituents, i.e., elastin, collagen, and smooth muscle cells (SMC), as well as their distributions are indispensable (Morales-Orcajo et al., 2018). In addition, such information is of high significance as input data for three-dimensional continuum mechanics-based models (Seydewitz et al., 2017).

The most common experiment on the UB to investigate its mechanical functions entails the observation of the entire organ during filling and micturition. This urodynamic, non-invasive in vivo testing technique, known as cystometry, is preferred in clinical practise (van Mastrigt et al., 1981; Andersson et al., 1989; Wall et al., 1994; Rohrmann et al., 1997; Damaser, 1999; Lee and Yoon, 2013; Nenadic et al., 2013; Takezawa et al., 2014; Bayat et al., 2017; Kim and Hill, 2017; Rocha, 2017). Furthermore, related studies range from classical cystometry analyses to more advanced methods, wherein the cystometrical setup is combined with different imaging techniques.

However, besides the previously mentioned advantages of cystometry, it cannot be used to determine layer- or position-dependent properties. To determine such characteristics, experiments on tissue strips dissected from the UB are indispensable. Generally, two types of experiments can be found in the literature.

On the one hand, uniaxial tension experiments (e.g. Finkbeiner and O'Donnell, 1990; Rohrmann et al., 1997; Dahms et al., 1998; Brown et al., 2002; Korossis et al., 2009; Martins et al., 2011; Zanetti et al.,

* Corresponding author.
E-mail address: m.boel@tu-bs.de (M. Böl).

https://doi.org/10.1016/j.jmbbm.2020.104275
Received 15 July 2020; Received in revised form 4 November 2020; Accepted 12 December 2020
Available online 18 December 2020

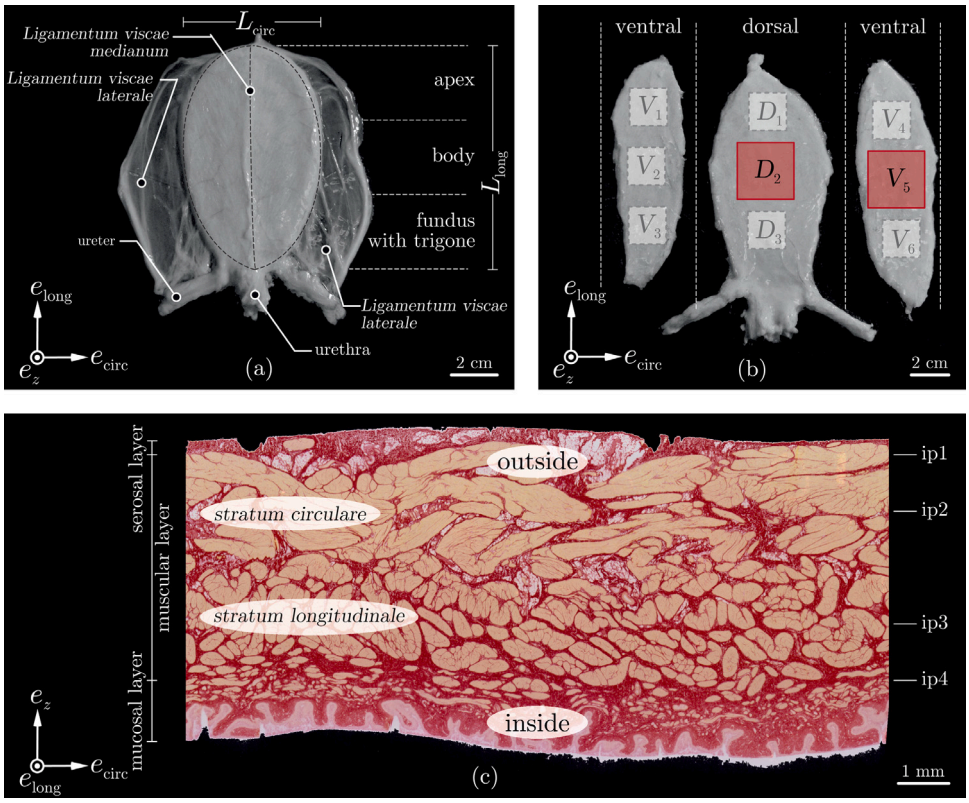

Fig. 1. Porcine bladder tissue sample dissection: (a) Top view of the deflated UB for measuring the projected dimensions (L_{long} and L_{circ}), (b) sample locations from the bladder's outside view (while red rectangles indicate samples which are used for mechanical testing, light grey dotted rectangles are dissection positions realised in Morales-Orcajo et al., 2018), and (c) cross-sectional view of the UBW with position details of the in-plane slices (ip1 to ip4) of the UBW.

2012; Barnes et al., 2015; Natali et al., 2015; Menzel et al., 2017; Seydewitz et al., 2017), which are relatively easy to perform, are frequently conducted. On the other hand, there are studies that have presented more complex biaxial tension experiments (Baskin et al., 1994; Gloeckner et al., 2002; Nagatomi et al., 2004, 2008; Lu et al., 2005; Gilbert et al., 2008; Toosi et al., 2008; Wang et al., 2009; Cheng et al., 2018; Morales-Orcajo et al., 2018). From a physiological perspective, the UB is in vivo subjected to biaxial deformations. Furthermore, experimental studies (e.g. Seydewitz et al., 2017; Morales-Orcajo et al., 2018) show that the mechanical behaviour of the UBW is apparently anisotropic. In addition to conducting biaxial experiments, orientation-dependent uniaxial studies are another alternative. However, only six studies have been conducted on orientation-dependent axial tension experiments (Korossis et al., 2009; Martins et al., 2011; Zanetti et al., 2012; Natali et al., 2015; Seydewitz et al., 2017; Borsdorf et al., 2019). Moreover, knowledge of the location-dependent properties is of particular importance for a more comprehensive understanding of UB mechanics, especially with respect to its function. Within the existing literature, only three investigations that focus on location dependency in reference to mechanical characteristics are available (Korossis et al., 2009; Morales-Orcajo et al., 2018; Borsdorf et al., 2019). No regional or directional differences were found in the active muscle properties, like force–length or force-velocity relations (Borsdorf et al., 2019). Interestingly, significant regional differences in passive mechanical characteristics of the UB wall were found by Korossis et al. (2009) and Morales-Orcajo et al. (2018) performing uniaxial and biaxial tensile experiments, respectively. However, for better mechanical understanding, as well as for the development of three-dimensional continuum mechanics-based models, information on layer-specific mechanical behaviour is of enormous importance. Even after intensive literature research, only one study has been found that deals with the layer-specific and mechanical characterisation of porcine UB tissue (Seydewitz et al., 2017). In the context of this study, uniaxial, and orientation-dependent investigations were conducted to clarify the different mechanical properties of the individual layers. However, biaxial layer-specific investigations are currently unavailable.

Microstructural information, such as fibre orientations and distributions of the different tissue constituents (elastin, collagen, and SMC), is essential for a better understanding of UB mechanics (Morales-Orcajo et al., 2018). In particular, the combination of microstructural and mechanical information is of high importance as it allows for the identification and better comprehension of the load transfer mechanisms that occur during organ loading and unloading. However, studies of this type are extremely rare. So far, only two studies have been found that address the mechanical and microstructural characterisation of UB tissues (Cheng et al., 2018; Morales-Orcajo et al., 2018). On the one hand, Cheng et al. (2018) combined biaxial mechanical testing with multiphoton microscopy, whereby the authors were able to match the percentage of collagen fibres straightened by the stress–strain relation of rat UBW specimens; on the other hand, Morales-Orcajo et al. (2018) performed biaxial tension experiments on porcine UB tissues and matched them with fibre bundle orientations/distributions and proportions of the tissue constituents (elastin, collagen, SMC).

2. Materials and methods

2.1. Structural aspects of urinary bladder soft tissue

The UBW consists of three main layers (from the inside out): The mucosal, muscular, and serosal layers, cf. Fig. 1(c). For a detailed description of the bladder wall microstructure, the reader is referred to Seydewitz et al. (2017). Summarily, the mucosal layer, which displays many thick folds in the empty state of the bladder, consists of three sublayers: The innermost transitional epithelium, lamina propria, and tunica submucosa. All these layers have different physiological and

Table 1
Number of tissue samples used within this studies for mechanical and histological investigations.

	Mechanics, set S_1		Histology (fibre orientation, set S_2)		Histology (layer thickness, set S_3)	
	D_2	V_5	D_2	V_5	D_2	V_5
Mucosal layer	5	5	–	–	–	–
Muscular layer	5	5	12	12	24	24

mechanical functions; they consist of collagen networks, some of which contain SMCs (tunica submucosa). The muscular layer consists of SMCs embedded in a collagen network and features various differentiable smooth muscle sublayers that are not very evident. In large areas of the UBW, the inner and outer sublayers are predominantly longitudinally (*Stratum longitudinale*) and circumferentially (*Stratum circulare*) oriented (e.g. Pel et al., 2005; Morales-Orcajo et al., 2018), cf. Fig. 1(c). The serosal layer is the outermost layer of the UBW, and features two sublayers: The innermost tela subserosa and the tunica serosa. In addition to the low elastin content at the interface between the muscular layer and tunica serosa and a network of autonomous nerve fibres, the serosal layer mainly consists of wavy collagen fascicles that form a loose network of fibres.

2.2. Ethical approval

The study was exempted from ethical committee review according to the National Regulations (German Animal Welfare Act), as porcine urinary bladders of healthy domestic pigs were obtained from a slaughterhouse immediately after animal sacrifice.

2.3. Urinary bladder sample dissection

In this study, twenty-nine ($n = 29$) UBs of domestic pigs (*Sus scrofa domestica*) that were 5–7 months old and approximately 90 kg in weight, were obtained from a slaughterhouse immediately after animal sacrifice and transported to the laboratory. During the transport and preparation, the organs were stored in calcium-free Krebs solution (Parekh et al., 2010: 113 mM NaCl, 4.7 mM KCl, 1.2 mM $MgSO_4$, 25 mM $NaHCO_3$, 1.2 mM KH_2PO_4, 5.9 mM dextrose, and 1 mM EGTA) to prevent spontaneous contractions, especially during the biaxial tensile experiments.

Before the UBs were mechanically tested, they were measured in their empty, relaxed state, see Fig. 1(a). The mean weight was found to be 45.9 ± 6.1 g and the average sizes were 91.2 ± 6.6 mm in projected length (L_{long}) and 58.3 ± 4.1 mm in projected width (L_{circ}). Following Fig. 1(b) and according to Morales-Orcajo et al. (2018), the UB was sliced along the *Ligamentum vesicae laterale* and *Ligamentum vesicae medianum*, dividing the bladder into three tissue parts indicated by D (dorsal) and V (ventral). Previous location-dependent mechanical investigations on UBs (Morales-Orcajo et al., 2018) indicated the largest differences in mechanical responses for samples D_2 and V_5 (red rectangles), which inspired the use of these samples for mechanical testing in the present study, see set S_1 in Table 1. The samples were dissected at identical positions for the realisation of histological investigations. To this end, the sample sets S_2 (twenty-four $n = 24$ samples) and S_3 (forty-eight $n = 48$ samples) were used for in-plane fibre orientation identification and thickness measurements, respectively. Thus, a total of ninety-two ($n = 92$) tissue samples were used in this study.

2.4. Sample processing and mechanical testing

For the realisation of equi-biaxial tension experiments, a testing machine (Zwick GmbH & Co. KG, Germany), featuring four linear actuators that can be controlled independently, was used, for details see Morales-Orcajo et al. (2018). Summarily, force was measured by load cells, two in each loading direction e_{circ} and e_{long}. A video extensometer (Video Extensometer ME46, Messphysik Materials Testing GmbH, Austria) was positioned above the tissue sample to track the markers on the specimen during testing. To control the actuator movement, the extensometer was coupled to the testing machine. For data analysis, see Section 2.5, load cell values, actuator positions, and marker displacements were recorded.

After dissecting the tissue samples (30×30 mm), nine markers were applied in a square-shaped area (6×6 mm) on the sample outside (to be identical to the outer surface of the UB) to allow deformation tracking during first mounting, preconditioning, layer separation, second mounting, and final testing. Following Morales-Orcajo et al. (2018), five hooks were inserted on each sample side, the specimen was positioned into the biaxial testing machine, and submerged in calcium-free Krebs solution at 37° C, while being continuously bubbled with a gas mixture of 95% O_2 and 5% CO_2, see Fig. 3. In a further step, the strips were preconditioned by 12 stretch-controlled loading/unloading cycles, ranging from $\lambda = 1.3$ to $\lambda = 1.4$ to achieve a stable reference state. For realising the preconditioning cycles, we followed Morales-Orcajo et al. (2018) and applied a preload in both axes to avoid weight effects, i.e., to guarantee the horizontal alignment of the samples, and therefore ensure the correct measurement of the initial markers distance in-plane. For layer separation, the preconditioned sample was cut into smaller square-shaped samples (20×20 mm), for dimensions see Appendix A, and fixed with needles on the polystyrene block with the mucosal layer underneath. A horizontal cut below the muscular layer was carefully performed with micro scissors under magnification glasses. The sample was kept at 45°, allowing gravity to peel off the muscular layer during cutting. The stretch of the muscular layer was tracked using the initially applied markers. Owing to the fixation of the mucosal layer with needles, no deformation was detected in this layer. After complete separation of the layers, nine markers were applied to the mucosal layer to optically track its deformation during biaxial sampling.

After layer separation, the single layers, i.e., the muscular and mucosal layers, were mechanically tested under a single equi-biaxial loading until tissue sample failure occurred by applying a strain rate of $\dot{\varepsilon} = 0.2\%/\text{s}$.

2.4.1. Reference state of urinary bladder specimen

In the undeformed state, the different layers of the UBW feature dissimilar waviness, see Fig. 2(a). The waviness is particularly pronounced in the mucosal layer, as seen in the enlargement in (a). However, in combination with various softness properties of the different layers, the mechanical responses might strongly depend on the (improper) handling history of the tissue. This particularly applies to the mucosal layer during preconditioning and layer separation. In this scenario, the layer might be elongated and thus, may not reflect its natural waviness as in the in vivo situation, which is defined as the mechanical reference state. To this end, the sampling history was tracked throughout the entire process: Before the sample was mounted for the first time into the test machine, the reference configuration was recorded using attached markers, see Fig. 3(a). Thereafter, 12 preconditioning cycles, cf. Fig. 4(b), were performed and the first pre-stretch $\lambda_{\text{pre},1}$ was measured accounting for preconditioning and mounting processes. Due to the layer separation, which necessitates the unmounting of the sample, the waves of the mucosal layer were pulled out. Both, the unmounting and the pull out of the waves, results in a further stretching $\Delta\lambda$, see Fig. 2(b). The total stretch $\lambda_{\text{pre},2}$, can thus be calculated from parts of first mounting, preconditioning, sample separation, and second mounting, see Fig. 2(b). While $\lambda_{\text{pre},2}$ is necessary for a clear characterisation of the mechanical behaviour of the UBW, $\lambda_{\text{pre},1}$ is only an auxiliary variable.

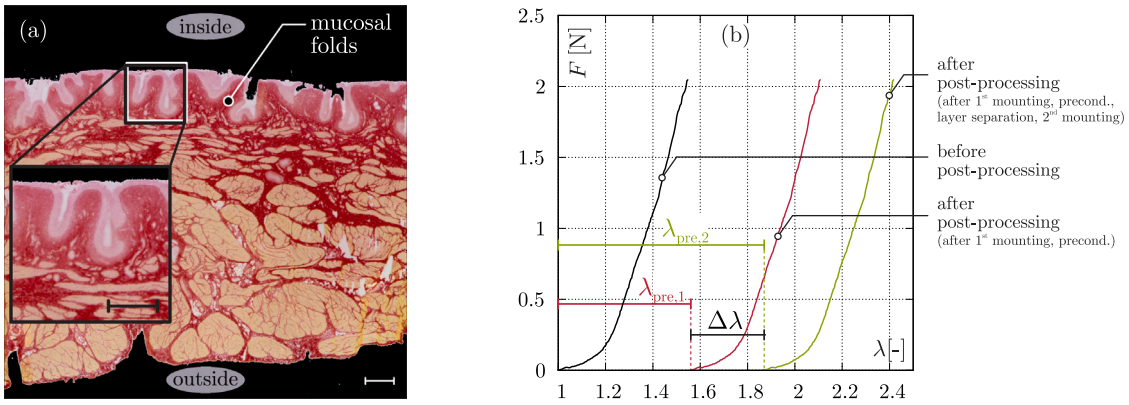

Fig. 2. UBW reference state and pre-stretch determination: (a) Histological cross-section of porcine UBW strained with Picro-Sirius red and (b) force–stretch response of the mucosal layer before post-processing (black line), after the first mounting and 12 cycles of preconditioning (red line), and after additional layer separation and second mounting into the testing machine (green line). Scale bar: 500 μm.

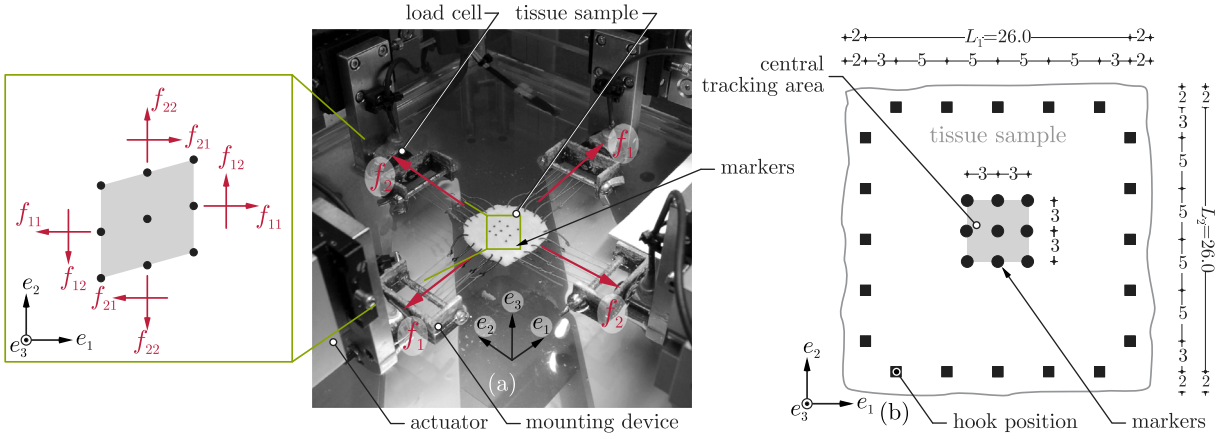

Fig. 3. Experimental, biaxial setup: (a) View of the tissue specimen mounted in the testing machine. (b) Idealised illustrations of the marker (filled circles) and hook (filled squares) positions. The forces acting on the tracked area are illustrated in the subfigure of (a). Note that the dimensions are given in millimetres, and the directions 1, 2, and 3 of the coordinate system correspond to the circumferential, longitudinal, and z-direction in Fig. 1, respectively.

2.5. Data analysis — determination of stresses and stretches

Following Fig. 3(a), while performing stretch-controlled equi-biaxial tension experiments, two forces (f_1 in the circumferential and f_2 in the longitudinal direction) were measured. Owing to the microstructural conditions of the UBW, shear forces are observed, leading to shear deformation. However, all forces (two normal f_{11} and f_{22}, and two shear forces f_{12} and f_{21}) acting on the tissue sample, see sub-figure of (a), are unknown. To determine these forces in the post-processing step, we follow the procedure presented in Morales-Orcajo et al. (2018), while assuming incompressible and homogeneous deformations within the central tracking area, see (b). Knowing the coordinates of all nine markers in the subfigure of (a), we obtain the stretches

$$\lambda_1 = \frac{\partial u_1}{\partial X_1} + 1,\ \lambda_2 = \frac{\partial u_2}{\partial X_2} + 1,\ \text{and}\ \lambda_3 = \frac{1}{\lambda_1\lambda_2 - \gamma_1\gamma_2} \tag{1}$$

and in-plane shear

$$\gamma_1 = \frac{\partial u_1}{\partial X_2}\ \text{and}\ \gamma_2 = \frac{\partial u_2}{\partial X_1}, \tag{2}$$

to be components of the deformation gradient $F_{ij} = \partial u_i/\partial X_j + \delta_{ij}$, determined from the displacement of the nine markers by means of isoparametric interpolation (Sommer et al., 2015). Therefore, u_i, X_i, and δ_{ij} are the displacements, reference coordinates, and Kronecker delta, respectively. By knowing the dimensions of the undeformed specimen in form of the lengths in both directions (L_1, L_2) and the thickness (T), as well as the forces acting on the tracked areas, as illustrated in Fig. 3, the normal stresses

$$\sigma_{11} = \lambda_1\frac{f_{11}}{L_2T} + \gamma_1\frac{f_{12}}{L_1T} := \sigma_{\text{circ}}\ \text{and}\ \sigma_{22} = \lambda_2\frac{f_{22}}{L_1T} + \gamma_2\frac{f_{21}}{L_2T} := \sigma_{\text{long}} \tag{3}$$

and shear stresses

$$\sigma_{12} = \lambda_2\frac{f_{12}}{L_1T} + \gamma_2\frac{f_{11}}{L_2T} = \lambda_1\frac{f_{21}}{L_2T} + \gamma_1\frac{f_{22}}{L_1T} = \sigma_{21} := \sigma_{\text{shear}} \tag{4}$$

can be calculated, see Morales-Orcajo et al. (2018).

Since every sample is stretched prior to testing and failures occur at various strains, each test features individual boundaries, thereby prohibiting the calculation of the average stress–stretch behaviour. Therefore, samples belonging to the same category (mucosal layer and muscular layer) were normalised by mapping the domain of the stress–stretch relation onto a unit interval, allowing the calculation of the mean and standard deviation. Thereafter, the average stress–stretch relation was transformed back to the interval $[1, \lambda_{\text{max,mean}}]$ by

$$g(\lambda) = (\lambda_{\text{max,mean}} - 1)\lambda + 1\ \text{ with }\ \lambda \in [0, 1]. \tag{5}$$

Herein, $\lambda_{\text{max,mean}}$ defines the average of the maximum stretches reached in the group of tests.

2.6. Smooth muscle fibre bundle distribution

To study the smooth muscle (SM) fibre distribution in the unloaded situation, as well as during tensile loading, tissue samples of set S_2 were histologically investigated. To this end, twenty-four ($n = 24$) rectangular samples from each of the two positions, D_2 and V_5, were directly

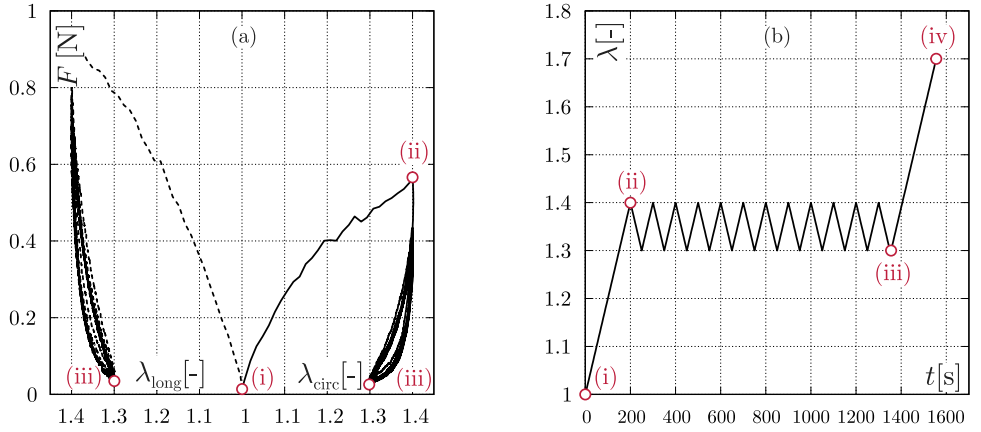

Fig. 4. Preconditioning protocol within the present study: (a) Representative tissue preconditioning response (dorsal specimen with entire wall structure) in the longitudinal (dashed lines) and circumferential (solid lines) directions through 12 successive stretch-controlled cycles, ranging from 1.3 to 1.4. (b) Stretch–time curve to which all samples were subjected. Note, the points (i), (ii), (iii), and (iv) describe characteristics point used later within the text.

fast-frozen after dissection by immersing them in liquid isopentane (−160° C), cooled with liquid nitrogen (−210° C), and stored at −80° C in an ultra-low freezer.

A cryomicrotome, cooled to −20° C (Fischer et al., 2008), was used to produce 6 μm thick sections: For thickness determination, one section per sample was used, and for in-plane fibre bundle orientation analysis within the muscular layer, four successive sections were utilised. The latter sections were distributed as illustrated in Fig. 1(c), i.e., two sections were each prepared in the *Stratum circulare* (ip1, ip2) and the *Stratum longitudinale* (ip3, ip4). The Picrosirius red staining protocol, see Appendix B, was used for SM fibre bundle visualisation. Histological sections were digitised via digital microscopy (ZEISS Smartzoom 5). The same method was applied to samples for thickness evaluation (set S_3), which led to a better visibility of different layers.

The orientation of the muscle fibre bundles was determined directly from the digitised image based on the evaluation of the structure tensor Bigun et al. (2004) within the region of interest. Calculations were performed according to Rezakhaniha et al. (2012), leading to a weighted orientation histogram with angles from −90° to 90°, cf. Fig. 7. The dominant fibre direction, represented by the structure tensor

$$\boldsymbol{Z} = \frac{1}{n}\sum_{i=1}^{n} \boldsymbol{m}_i \otimes \boldsymbol{m}_i \tag{6}$$

was identified by reducing the angle data from the histogram. Herein, $\boldsymbol{m}_i$ are the directional vectors of the corresponding angle α_i, and n defines the number of considered angles. With the eigenvectors and eigenvalues of $\boldsymbol{Z}$ available, the eigenvector with the largest corresponding eigenvalue indicates the dominant direction vector $\boldsymbol{m}_\mathrm{d}$. By establishing the linear decomposition

$$\boldsymbol{m}_\mathrm{d} = a_1\boldsymbol{e}_1 + a_2\boldsymbol{e}_2 \tag{7}$$

of $\boldsymbol{m}_\mathrm{d}$, the corresponding angle

$$\alpha_\mathrm{d} = \tan^{-1}\left(\frac{a_1}{a_2}\right) \tag{8}$$

depends on the vector coefficients a_1 and a_2.

2.7. Micromechanical load transfer mechanisms in the urinary bladder wall

Based on the complex microstructure of UBWs, it is easy to see that there is an extensive interplay between the individual layers under mechanical loading. For example, UBWs typically feature low internal pressures, even with a large filling volume (Parekh et al., 2010; Parsons et al., 2012; Habteyes et al., 2017). This is due to the microstructure of the UBW and its specific load-transfer mechanisms, which remain unexplored.

To gain insight into these mechanisms, samples from the dorsal and ventral regions were loaded equi-biaxially up to certain degrees of elongation of $\lambda = 1.0/1.3/1.5/1.6/1.7/1.8/2.0$ and then, fast-frozen in their deformed state. In doing so, we followed a protocol described in Morales-Orcajo et al. (2018). Comprehensively, after biaxially stretching the tissue sample, thin metal pins, attached to a rigid frame, were pressed into the deformed tissue around the region of interest, such that it could no longer deform mechanically. Subsequently, the tissue, still fixed to the frame, was fast-frozen. Microstructural changes were assessed by comparing the histological cross-sections of the unloaded and loaded sample sections. From the unloaded and loaded samples, the average thickness values, T_unloaded and T_loaded, were measured in the dorsal and ventral regions at two positions for four samples each, leading to the attainment of the average behaviour of sixteen samples. Finally, the thinning response was calculated as

$$\mathcal{T} = \left(1 - \frac{T_\mathrm{loaded}}{T_\mathrm{unloaded}}\right) \times 100. \tag{9}$$

A total of forty-eight samples were evaluated, and four samples were tested at two locations for six stretch levels.

3. Results

3.1. Urinary bladder mechanical properties

Before measuring the mechanical properties of the individual tissue layers, tissue strips featuring the entire wall structure were preconditioned. In Fig. 4, typical preconditioning cycles during equi-biaxial loading based on force vs. stretch are illustrated. Interestingly, the first loading curve features a convex behaviour, while all other loading and unloading curves are characterised by concave curve progressions. During the first four to six preconditioning cycles, a change in the maximum force is evident. Between cycles 8 and 12, the curves are stable and exhibit reproducible behaviour, which is characterised by a distinct exponential course and significantly differs from the first load path (from $\lambda = 1.0$ to $\lambda = 1.4$). Furthermore, in the longitudinal direction, the material behaviour is significantly stiffer compared to the circumferential direction ($F = 0.92$ N and $F = 0.56$ N).

After separating the mucosal and muscular layers, the specimen was loaded up to failure limit, which was usually expressed by tearing off the hooks. In Fig. 5, the mean values (lines) and standard deviations (shaded areas) of layer-specific tests are presented in terms of Cauchy stress vs. stretch for the two different locations (D_2, V_5). Regardless of the sample position, the tissue strips exhibit similar qualitative properties, which are characterised by an exponential and non-linear behaviour. Irrespective of the dissection position, the stresses in the longitudinal direction (dashed lines) appear to be marginally higher than

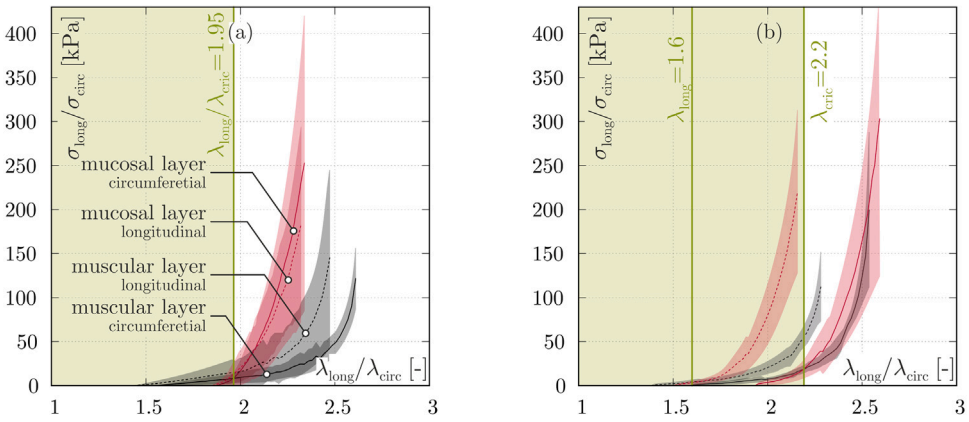

Fig. 5. Layer- and orientation-specific stress–stretch behaviours of the UBW: Experiments on the (a) dorsal and (b) ventral region. Curves characterise mean values while shaded areas depict standard deviations.

Table 2
Direction- and position-dependent pre-stretches $\lambda_{pre,1}$ and $\lambda_{pre,2}$ (mean ± s.d.).

	$\lambda_{pre,1}$		$\lambda_{pre,2}$			
	Entire strip		Muscle layer		Mucosal layer	
	D_2	V_5	D_2	V_5	D_2	V_5
Circumferential direction	1.37 ± 0.19	1.38 ± 0.11	1.56 ± 0.35	1.59 ± 0.16	1.87 ± 0.18	1.94 ± 0.11
Longitudinal direction	1.35 ± 0.17	1.21 ± 0.10	1.44 ± 0.16	1.38 ± 0.14	1.85 ± 0.27	1.50 ± 0.16

in the circumferential direction (solid lines). The stretch-dependent stiffness values of the different layers are rather interesting. Regardless of the loading direction, the dorsal specimens (a) show that, up to a stretch of $\lambda_{long} = \lambda_{circ} = 1.95$ (green area), the muscular layer exhibits a stiffer behaviour compared to the mucosal layer. Above a stretch of $\lambda_{long} = \lambda_{circ} = 1.95$, the stiffness of the mucosal layer significantly increases in both directions, exceeding the stiffness of the muscular layer. For the ventral specimens (b), the circumferential and longitudinal directions (green area) are similar up to a stretch of $\lambda_{circ} = 2.2$ or $\lambda_{long} = 1.6$, i.e., the muscular layer is stiffer compared to the mucosal layer. For larger stretches, the mucosal layer increases significantly in stiffness, as also apparent in the dorsal area. Under physiological conditions, UBs are stretched by 90% to 130% (rat UB Parekh et al., 2010), and thus, the stiffness ratios are approximately as in the area marked green in Fig. 5; the findings gained here are of particular importance. Consequently, it seems that under physiological conditions, the muscular layer is the first to transfer loads followed by the mucosal layer at higher stretches.

During the entire processing of the tissue (first mounting, preconditioning, layer separation, and second mounting), the sample length changes were monitored, indicated by the nine markers at the centre of the sample. These lengths were converted into pre-stretches ($\lambda_{pre,1}$ and $\lambda_{pre,2}$), as shown in Table 2. However, the second pre-stretch $\lambda_{pre,2}$ consistently exhibits a higher value than the first one $\lambda_{pre,1}$. Generally, the pre-stretch of the mucosal layer is evidently higher than that of the muscular layer. Nonetheless, shifting the measured stress–stretch relations based on the determined pre-stretched $\lambda_{pre,2}$, leads to the shifted relations, as illustrated in Fig. 5.

As a quantitative measure of directional dependencies, the degree of anisotropy (Sommer et al., 2015)

$$\xi = \frac{|\sigma_{11} - \sigma_{22}|}{\max(\sigma_{11}, \sigma_{22})} \tag{10}$$

is introduced, ranging between zero and unity for fully isotropic and anisotropic behaviours, respectively. In Table 3, the degree of anisotropy is presented as a function of layer and region. The mean values for the muscular layer were higher than those for the mucosal layer. Furthermore, regional differences can be identified; the degree of anisotropy is higher in the dorsal than in the ventral region, irrespective of the layer. Deviations from the mean value are, except for the dorsal mucosal layer, high, indicating large differences between samples of the same region and layer.

Table 3
Degree of anisotropy (mean ± s.d.) in dependence of the region and the layer.

muscular layer		mucosal layer	
D_2	V_5	D_2	V_5
0.45 ± 0.22	0.38 ± 0.20	0.30 ± 0.06	0.24 ± 0.16

Table 4
Data (mean ± s.d.) for maximum shear stress normalised to maximal normal stress in different regions and layers in percent and in-plane shear.

		Muscle layer		Mucosal layer	
		D_2	V_5	D_2	V_5
$\sigma_{shear}/\sigma_{circ}$	[%]	1.43 ± 2.24	5.93 ± 5.14	0.25 ± 0.34	3.54 ± 2.92
$\sigma_{shear}/\sigma_{long}$	[%]	2.62 ± 3.77	3.75 ± 2.65	0.19 ± 0.24	2.49 ± 1.71
γ_{circ}	[–]	0.13 ± 0.13	0.20 ± 0.13	0.22 ± 0.20	0.14 ± 0.10
γ_{long}	[–]	0.15 ± 0.09	0.17 ± 0.09	0.15 ± 0.07	0.12 ± 0.06

Shear stresses (σ_{shear}) and in-plane shear ($\gamma_{circ/long}$) for both regions and layers are listed in Table 4. Large deviations prohibit the interpretation of these values with respect to the different locations and layers. The impact of shear stress is negligible, except for a single test in the ventral muscular layer, which leads to an increased mean value. In particular, the dorsal mucosal layer exhibits a very low fraction of shear to normal stress. For each layer and region, a higher in-plane shear corresponds to a higher fraction of stresses.

3.2. Urinary bladder microstructure

3.2.1. Microstructural changes under loading conditions

An essential question with regard to tissue engineering entails how loads are transferred within the UBW. The partly wavy structure of the muscular and mucosal layers, see Fig. 1, plays a pivotal role in this process. To shed more light on this question, the thinning responses of cross-sections (averaged over dorsal and ventral regions) under increasing tension deformation were analysed, see Fig. 6. At a maximum

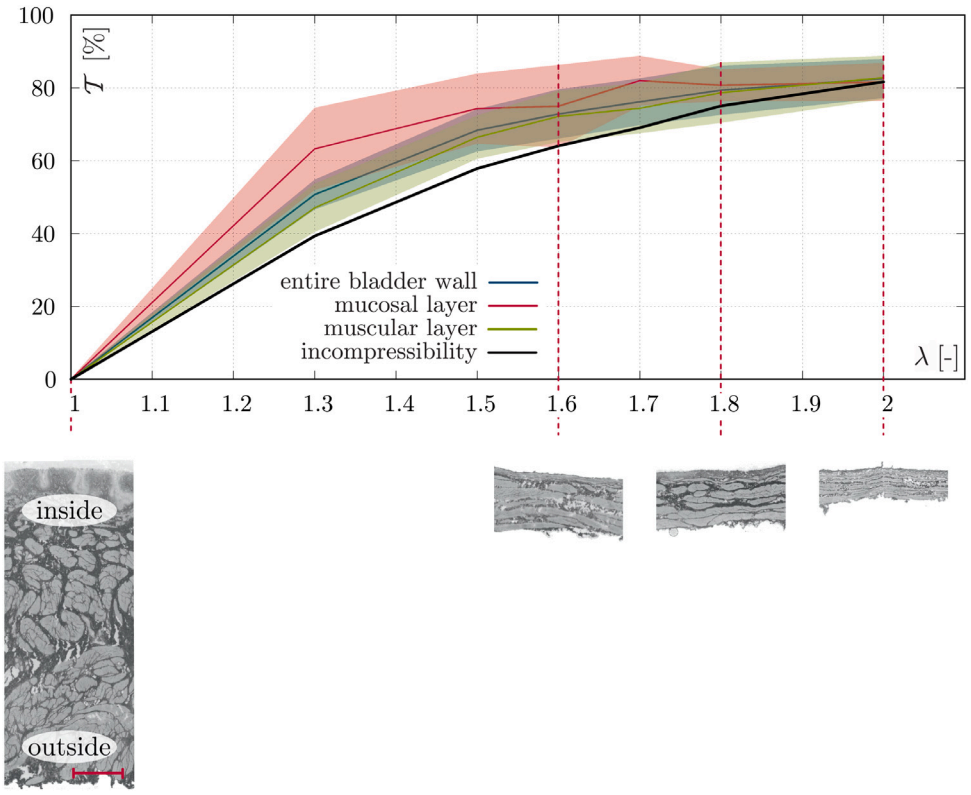

Fig. 6. Layer-specific thinning characteristics of the UBW at discrete stretch levels $\lambda = 1.0/1.3/1.5/1.6/1.7/1.8/2.0$. The solid curves characterise mean values while shaded areas depict standard deviations. Histological images are shown for stretch levels of $\lambda = 1.0/1.6/1.8/2.0$. Scale bar: 1 mm.

elongation of $\lambda = 2.0$, a thickness reduction of approximately 80% is more or less evident for all layers. This high thickness reduction is also apparent in the histological sectional images. While all curves exhibit a slightly compressible behaviour during the load paths, at maximum deformation, the averaged curves coincide with the theoretical value of incompressibility.

3.2.2. Smooth muscle fibre bundle orientation

Measurements of the fibre bundle orientations before and during loading as a function of the regions are shown in Fig. 7. In the first column, the orientations prior to loading are illustrated to be comparable to point (i) in Fig. 4(b). The various grey shades of the curves are associated with the depth of the in-plane section (ip1–ip4), i.e., with respect to Fig. 1(c). Thus, while ip1 presents the fibre bundle distribution in the outermost, ip4 displays the distribution of the innermost sections. Before testing (first column), in the dorsal region, the fibre bundles in the outermost section are circumferentially oriented, while they are longitudinally inclined in the innermost section. For the ventral region, the muscle fibres are generally more aligned in the oblique direction because the dominant fibre direction lies at −50° and 70° for the inner and outer layers, respectively. These results are consistent with the findings of Morales-Orcajo et al. (2018).

During further loading up to $\lambda = 1.4$, see point (ii) in the loading history in Fig. 4(b), the majority of the fibres in the dorsal region properly align themselves in the circumferential direction. This applies, more or less, to all layers. Furthermore, with increasing load ($\lambda = 1.3$ and 1.7), a change from a unimodal to a bimodal distribution is evident. This effect is particularly pronounced at maximum deformation ($\lambda = 1.7$, cf. point (iv) in Fig. 4(b)), where 50% of the samples have a dominant fibre bundle orientation in the longitudinal direction and the other half is oriented in the circumferential direction.

In the ventral region, multimodal distributions are measured, except for the outermost sections, which show reproducible results for different stretch states. During the deformation process, fibres of all layers (except the innermost layer) align themselves to an approximately identical orientation, i.e., to an orientation of −30°. At this point, it is particularly interesting to study the development of fibre orientation via the deformation process. In the undeformed state, the fibres of the outer layer ip1 have a dominant direction of −47°, while the orientation of the other layers (ip2–ip4) gradually change in positive direction, resulting in a dominant fibre direction of 70° for the innermost layer ip4. During sample deformation, the ip1 develops a dominant fibre orientation of approximately −27° while the ip4 changes to −45°.

4. Discussion

While many studies have emphasised the importance of layer-specific studies for different tissues, e.g., arteries (Lu et al., 2004; Holzapfel et al., 2005), stomach (Zhao et al., 2008; Jia et al., 2015; Bauer et al., 2020), small intestine (Sacks and Gloeckner, 1999; Lu et al., 2005), or oesophageal tissue (Natali et al., 2009; Sommer et al., 2013), only two studies conducted by Gilbert et al. (2008) and Seydewitz et al. (2017) have focused on the mechanical characteristics of various layers and their combinations via axial and biaxial tension experiments.

Although we investigated the mechanical characteristics of the entire UBW (Seydewitz et al., 2017; Morales-Orcajo et al., 2018) in previous works, biaxial tension experiments on the mucosal and muscular layer were performed in this study. Additionally, layer-specific pre-stretches were identified, which were important for understanding and interpreting load transfer mechanisms inside the UBW. We observed higher pre-stretches in the mucosal layer than in the muscular layer, which supported the idea of a low-stress unfolding process, as previously reported for mouse UB (Hornsby et al., 2017) and stomach tissues (Bauer et al., 2020). Hornsby et al. (2017) described a totally flattened state for a stretch of $\lambda = 1.8$, which approximately coincided with the onset of the present study.

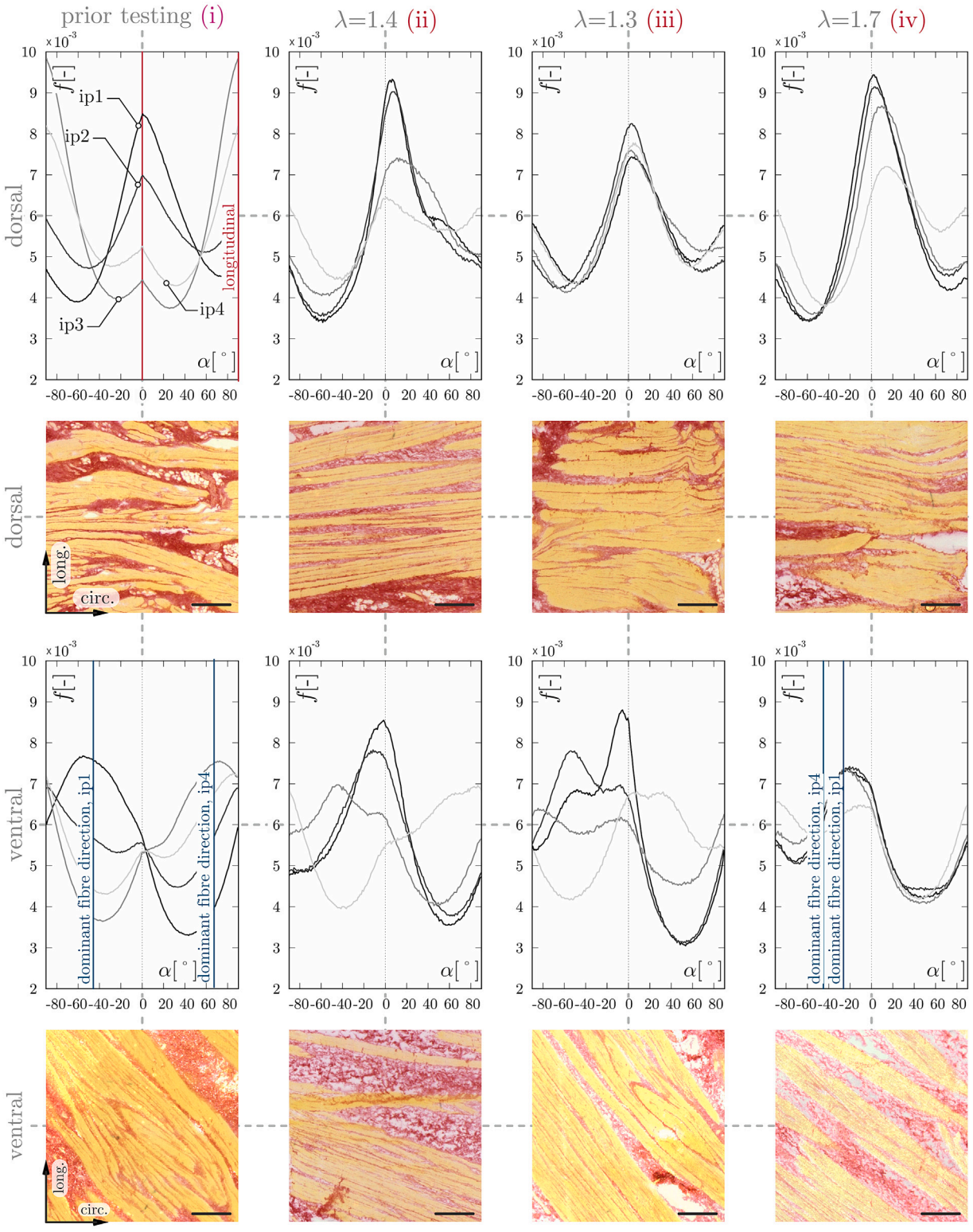

Fig. 7. Histograms of fibre bundle orientation distributions (orientation α versus fraction f) in dependence on tissue loading and sample location and representative in-plane histological images (stained with Picro-Sirius red, cf. Appendix B). In the first column, the orientations prior loading are illustrated. The fibre orientation at maximum ($\lambda = 1.4$) and minimum stretch ($\lambda = 1.3$) during cycling are illustrated in the second and third columns, respectively. Finally, in the last column, the distribution at maximum stretch ($\lambda = 1.7$) is illustrated. Notably, with respect to Fig. 1, a fibre bundle angle of 0° presents the circumferential and 90° the longitudinal direction. ip1 to ip4 represent the 4 in-plane sections of the muscular layer, cf. Fig. 1(c). Note, (i), (ii), (iii), and (iv) refer to the characteristic points defined in Fig. 4. Scale bars: 500 μm.

4.1. Urinary bladder mechanical properties

Performing layer-specific biaxial tension experiments revealed a stiffer behaviour of the thin mucosal layer, especially for higher stretches, leading to a comparable load bearing ability of both layers in the passive state of the muscular layer. For comparing low to moderate stretches (dorsal region: $\lambda = 1.95$, ventral region: $\lambda = 1.6$ to 2.2, cf. Fig. 5) based on typical physiological ranges during UB filling (Parekh

et al., 2010), the muscular layer features stiffer characteristics. However, high stiffness characteristics were also observed in the inner layer by Li et al. (2014), who performed layer-specific studies on rat UBs. In agreement with our results, investigations on stomach revealed lower stiffness at lower stretches in the mucosal layer than in the muscular layer (Dargar et al., 2017, 2019; Jia et al., 2015). This was also indirectly mentioned in Bauer et al. (2020) as the authors observed a larger pre-stretch in the mucosal layer, as performed in the present study. For large stretches, location dependency was observed for the stomach, while the UB appeared to exhibit a stiffer mucosal layer at both tested locations, which was slightly more pronounced in the central dorsal position.

The mucosal layer protects the muscular layer against urine and serves for sensing (Fry and Vahabi, 2016). Additionally, the present findings demonstrate the mechanical importance of the thin mucosal layer, as the exerted force is similar to that of the muscular layer. However, the higher pre-stretch of the mucosal layer indicates a softer behaviour than the muscular layer at low stretches, thereby supporting the theory of an unfolding process, as mentioned for the stomach (Bauer et al., 2020).

As there is no standardised testing protocol for biaxial tension experiments, a quantitative comparison with other studies is very difficult. However, in a previous study by Morales-Orcajo et al. (2018), the same preconditioning protocol was used, and a cyclic test was performed up to a total stretch of $\lambda = 1.7$. Interestingly, the first loading curve features a convex behaviour, while all other loading and unloading curves are characterised by concave curve progressions. In comparison to Morales-Orcajo et al. (2018), the curve progress of the first loading seems to be untypical, as in Morales-Orcajo et al. (2018) a concave progression was recorded. The reason for this difference is unclear and may have its cause in the variability of the biological tissue. Furthermore, the mechanical response of the muscular layer is lower than that of the entire wall at the same stretch Morales-Orcajo et al. (2018). This is mainly due to the additional pre-stretch, which is only recorded in the present study. Cheng et al. (2018) sampled rat UBs after five preconditioning cycles and obtained a similar stress response between 50 kPa and 150 kPa. Other studies observed a stiffer rat UB response (Gloeckner et al., 2002; Toosi et al., 2008; Wang et al., 2009; Chen et al., 2013). However, the specimens were stored in cooled physiological solutions prior to testing, making the direct comparison of the results very difficult.

4.2. Urinary bladder microstructure

One of the aims of this study was to determine the changes in thickness over different stretch states during loading and unloading. Because of the high liquid content of the bladder tissue (e.g. Natali et al., 2015), for the evaluation of experimental data, as well as for constitutive model development, the deformation kinematics are frequently assumed to be incompressible (e.g. Gloeckner et al., 2002; Seydewitz et al., 2017; Cheng et al., 2018; Jokandan et al., 2018). The method employed to measure the volume in the present study has the advantage of capturing the stretched state, while other methods, such as weighting of samples, only measure changes in the unloaded state; therefore, they inhibit the measurement of the dynamic changes in the inflow and outflow of fluids from the tissue. Nevertheless, the chosen approach results in a high standard deviation, which makes conveying a detailed description or conclusion difficult.

Changes in the dominant fibre orientation in the dorsal part are not expected, as the sample is stretched along the two fibre directions. This holds true for the outer muscular layer. The similarity between measurements before and after testing is remarkable given the second manual processing step of removing and freezing the sample. Cheng et al. (2018) studied the collagen fibre orientation of rat UBs in equi-biaxial tension experiments. The induced stretch leads to a straightening of collagen fibres and reduces its variance in the longitudinal direction (Cheng et al., 2018). This effect was not observed for SM fibres.

Fibres that are unaligned with the direction of deformation lead to a shift of the dominant orientation towards the longitudinal direction. This indicates a loose connection between fibres and the connective tissue, as the structure partially changes. This effect has already been observed for low stretches; however, the results for the dorsal region indicate a good measurement quality, as changes are not caused systematically by sample handling. These statements are valid for the outer layer.

The quality of the in-plane sections was drastically reduced for highly stretched tissue samples. A possible explanation is that the internal stresses destroy the 6 μm thick sections after thawing, during the staining process. The applied stretches at the end of the measurements, when referenced to the undeformed configuration, exceed common levels in biaxial experimental investigations (Nagatomi et al., 2005; Gloeckner et al., 2002; Wang et al., 2009; Cheng et al., 2018).

The large deviations between the same position, stretch, and cutting depth, as well as similarities between cutting depths at the same stretch, lead to the conclusion that the sections in both layers of the muscular layer are not exactly sliced. The thickness reduction, described theoretically in Fig. 6, plays a major role in the practical handling of the samples. Starting from an average thickness of approximately 6 mm, the resulting thin muscular layer at a thinning of $\mathcal{T} = 80\%$ (1.2 mm) is sectioned at four equidistant positions. Therefore, a misplacement of 2° of the 10 × 10 mm specimen in the microtome leads to an overlap of the initially defined sections. The physically unexplainable deviations are the result of high accuracy requirements for practical applications.

4.3. Functional aspects related to mechanical findings

Biaxial testing is common for hollow organs and allows for the attainment of a similar deformation state caused by UB filling (Morales-Orcajo et al., 2018). Based on the assumption that the UB is a sphere with an incompressible wall, the inner layer is stretched at an increased level when compared to the outer layer for the filling process of the entire organ. This underlines the mechanical importance of the mucosal layer displayed in Fig. 5.

The muscle fibre orientation in the ventral region is aligned towards the circumferential direction. Since the muscle fibre orientation indicates the direction of the contraction, a softer mechanical behaviour is expected during passive extension. However, a weak anisotropic condition for the dorsal and a stronger one for the ventral region was observed in this study, as well as in other works on tissue strips (Gloeckner et al., 2002; Morales-Orcajo et al., 2018; Cheng et al., 2018), while tests on whole organs revealed an increased stretch in the longitudinal direction during filling (Parekh et al., 2010). Therefore, the alignment is probably caused by the increased pre-stretch in the circumferential direction.

In the filling experiments, a stretch of $\lambda = 1.9$ in the circumferential and $\lambda = 2.3$ in the longitudinal directions was observed for rat UBs at a typical voiding volume of 0.74 ml (Parekh et al., 2010). In the present study, a stiffer material response of the mucosal layer coincides with the above-mentioned range, indicating a point of increased importance and very likely triggering the sensing function of this layer. This information has to be treated with caution, as the experiments by Parekh et al. (2010) were performed on rat UBs, and it is questionable whether the mechanical behaviour can be compared to that of porcine UBs.

4.4. Impact on urinary bladder modelling

Proving the assumption of incompressibility was not possible; however, a similar behaviour in all layers was observed, irrespective of the stretch. This indicates a homogeneous deformation state across the different layers, which leads to the assumption that different layers are described with the same volumetric part of the strain energy

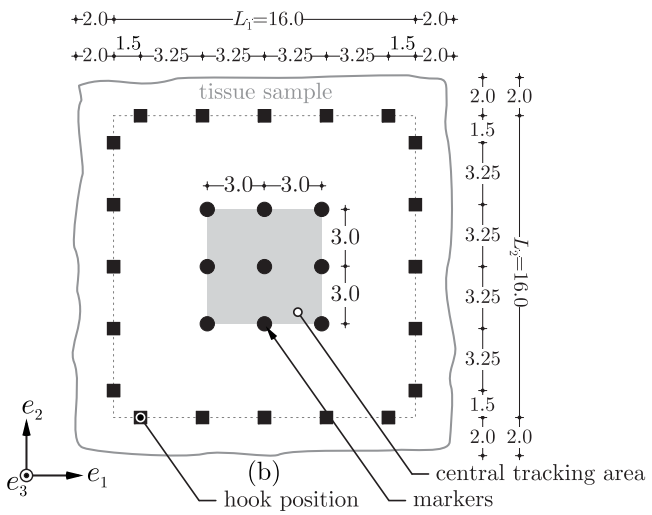

Fig. 8. Idealised illustrations of the marker (filled cycles) and hook (filled squares) positions. Note, the dimensions are given in millimetres.

function (Seydewitz et al., 2017) or constant Poisson ratio (Li et al., 2014).

Active and passive modelling approaches can utilise the obtained mechanical data of the mucosal layer. Previous works by Seydewitz et al. (2017) used the difference between an intact UBW and the muscular layer to gain insights into the mucosal layer. Uniaxial tension experiments revealed an equivalent mechanical load bearing capacity of the two layers, thereby supporting the previously made statement with regard to homogeneous deformation with minimal interaction between the layers.

CRediT authorship contribution statement

Robin Trostorf: Wrote the paper, Conducted the experiments and analysed the data. **Enrique Morales-Orcajo:** Conducted the experiments and analysed the data. **Tobias Siebert:** Coordinated the study. **Markus Böl:** Designed and coordinated the study, Wrote the paper.

Declaration of competing interest

The authors declare that they have no known competing financial interests or personal relationships that could have appeared to influence the work reported in this paper.

Acknowledgements

This work was supported by the Deutsche Forschungsgemeinschaft, Germany (DFG) under Grants BO 3091/9-1 and SI 841/9-1. The authors would like to thank Shuo Hao for assisting in lab repetitive tasks necessary to conduct the study. All authors analysed and discussed the results, and commented on the manuscript.

Appendix A. Marker and hook positions for tissues samples (20 × 20 mm)

Optical marker and hook positions for a tissue sample with 20 mm edge length (see Fig. 8).

Appendix B. Picro-Sirius red staining protocol for porcine urinary bladder wall (Morales-Orcajo et al., 2018)

1. Fix sections with Picro-Formalin for 5 min.
2. Rinse sections under gently running water for 10 min.
3. Stain sections with Picro-Sirius red solution for 60 min.
4. Rinse sections with acidified water for 2 min 2 times.
5. Rinse sections with distilled water for 1 min.
6. Dehydrate sections with ethanol 96% for 1 min.
7. Dehydrate sections with isopropanol for 1 min 2 times.
8. Clear sections with xylene for 5 min.
9. Cover sections with a mounting medium.

References

Andersson, S., Kronström, A., Bjerle, P., 1989. Viscoelastic properties of the normal human bladder. Scand. J. Urol. Nephrol. 23 (2), 115–120.
Barnes, S.C., Shepherd, D.E., Espino, D.M., Bryan, R.T., 2015. Frequency dependent viscoelastic properties of porcine bladder. J. Mech. Behav. Biomed. Mater. 42 (1), 168–176.
Baskin, L., Meaney, D., Landsman, A., Zderic, S.A., Macarak, E., 1994. Bovine bladder compliance increases with normal fetal development. J. Urol. 152 (2), 692–695.
Bauer, M., Morales-Orcajo, E., Klemm, L., Seydewitz, R., Fiebach, V., Siebert, T., Böl, M., 2020. Biomechanical and microstructural characterisation of the porcine stomach wall: Location- and layer-dependent investigations. Acta Biomater. 102 (1), 83–99.
Bayat, M., Kumar, V., Denis, M., Webb, J., Gregory, A., Mehrmohammadi, M., Cheong, M., Husmann, D., Mynderse, L., Alizad, A., Fatemi, M., 2017. Correlation of ultrasound bladder vibrometry assessment of bladder compliance with urodynamic study results. PLoS One 12 (6), e0179598.
Bigun, J., Bigun, T., Nilsson, K., 2004. Recognition by symmetry derivatives and the generalized structure tensor. IEEE Trans. Pattern Anal. Mach. Intell. 26 (12), 1590–1605.
Borsdorf, M., Tomalka, A., Stutzig, N., Morales-Orcajo, E., Böl, M., Siebert, T., 2019. Locational and directional dependencies of smooth muscle properties in pig urinary bladder. Front. Physiol. 10, 63.
Brown, A.L., Farhat, W., Merguerian, P.A., Wilson, G.J., Khoury, A.E., Woodhouse, K.A., 2002. 22 week assessment of bladder acellular matrix as a bladder augmentation material in a porcine model. Biomaterials 23 (10), 2179–2190.
Chen, J., Drzewiecki, B.A., Merryman, W.D., Pope, J.C., 2013. Murine bladder wall biomechanics following partial bladder obstruction. J. Biomech. 46 (15), 2752–2755.
Cheng, F., Birder, L.A., Kullmann, F.A., Hornsby, J., Watton, P.N., Watkins, S., Thompson, M., Robertson, A.M., 2018. Layer-dependent role of collagen recruitment during loading of the rat bladder wall. Biomech. Model. Mechanobiol. 17 (2), 403–417.
Dahms, S.E., Piechota, H.J., Dahiya, R., Lue, T.F., Tanagho, E.A., 1998. Composition and biomechanical properties of the bladder acellular matrix graft: Comparative analysis in rat, pig and human. Brit. J. Urol. 82 (3), 411–419.
Damaser, M.S., 1999. Whole bladder mechanics during filling. Scand. J. Urol. Nephrol. 33 (201), 51–58.
Dargar, S., Akyildiz, A.C., De, S., 2017. In situ mechanical characterization of multilayer soft tissue using ultrasound imaging. IEEE Trans. Biomed. Eng. 64 (11), 2595–2606.
Dargar, S., Kruger, U., De, S., 2019. In vivo layer-specific mechanical characterization of porcine stomach tissue using a customized ultrasound elastography system. J. Biomech. Eng. 141 (10), 1010041–10100410.
Finkbeiner, A.E., O'Donnell, P.D., 1990. Responses of detrusor smooth muscle to stretch and relaxation: In vitro study. Urology 36 (2), 193–198.
Fischer, A.H., Jacobson, K.A., Rose, J., Zeller, R., 2008. Cryosectioning tissues. Cold Spring Harbor Prot. 3 (8), 1–2.
Fry, C.H., Vahabi, B., 2016. The role of the mucosa in normal and abnormal bladder function. Basic Clin. Pharmacol. Toxicol. 119 (3), 57–62.
Gilbert, T.W., Wognum, S., Joyce, E.M., Freytes, D.O., Sacks, M.S., Badylak, S.F., 2008. Collagen fiber alignment and biaxial mechanical behavior of porcine urinary bladder derived extracellular matrix. Biomaterials 29 (36), 4775–4782.
Gloeckner, D.C., Sacks, M.S., Fraser, M.O., Somogyi, G.T., de Groat, W.C., Chancellor, M.B., 2002. Passive biaxial mechanical properties of the rat bladder wall after spinal cord injury. J. Urol. 167 (5), 2247–2252.
Habteyes, F.G., Komari, S.O., Nagle, A.S., Klausner, A.P., Heise, R.L., Ratz, P.H., Speich, J.E., 2017. Modeling the influence of acute changes in bladder elasticity on pressure and wall tension during filling. J. Mech. Behav. Biomed. Mater. 71, 192–200.
Holzapfel, G.A., Sommer, G., Gasser, C.T., Regitnig, P., 2005. Determination of layer-specific mechanical properties of human coronary arteries with nonatherosclerotic intimal thickening and related constitutive modeling. Am. J. Physiol.-Heart Circ. Physiol. 289 (5), H2048–2058.

Hornsby, J., Daly, D.M., Grundy, D., Cheng, F., Robertson, A.M., Watton, P.N., Thompson, M.S., 2017. Quantitative multiphoton microscopy of murine urinary bladder morphology during in situ uniaxial loading. Acta Biomater. 64, 59–66.

Jia, Z.G., Li, W., Zhou, Z.R., 2015. Mechanical characterization of stomach tissue under uniaxial tensile action. J. Biomech. 48 (4), 651–658.

Jokandan, M.S., Ajalloueian, F., Edinger, M., Stubbe, P.R., Baldursdottir, S., Chronakis, I.S., 2018. Bladder wall biomechanics: A comprehensive study on fresh porcine urinary bladder. J. Mech. Behav. Biomed. Mater. 79, 92–103.

Kim, A.K., Hill, W.G., 2017. Effect of filling rate on cystometric parameters in young and middle aged mice. Bladder 4 (1), e28.

Korossis, S., Bolland, F., Southgate, J., Ingham, E., Fisher, J., 2009. Regional biomechanical and histological characterisation of the passive porcine urinary bladder: Implications for augmentation and tissue engineering strategies. Biomaterials 30 (2), 266–275.

Lee, T., Yoon, S.M., 2013. The role of intra-abdominal pressure measurement in awake rat cystometry. Int. Neurourol. J. 17 (2), 44–47.

Li, C., Guan, G., Zhang, F., Song, S., Wang, R.K., Huang, Z., Nabi, G., 2014. Quantitative elasticity measurement of urinary bladder wall using laser-induced surface acoustic waves. Biomed. Opt. Express 5 (12), 4313–4328.

Lu, X., Pandit, A., Kassab, G.S., 2004. Biaxial incremental homeostatic elastic moduli of coronary artery: Two-layer model. Am. J. Physiol.-Heart Circ. Physiol. 287 (4), H1663–1669.

Lu, S.H., Sacks, M.S., Chung, S.Y., Gloeckner, D.C., Pruchnic, R., Huard, J., de Groat, W.C., Chancellor, M.B., 2005. Biaxial mechanical properties of muscle-derived cell seeded small intestinal submucosa for bladder wall reconstitution. Biomaterials 26 (4), 443–449.

Martins, P.A., Silva Filho, A.L., Fonseca, A.M., Santos, A., Santos, L., Mascarenhas, T., Jorge, R.M., Ferreira, A.J., 2011. Uniaxial mechanical behavior of the human female bladder. Int. Urogynecol. J. 22 (8), 991–995.

van Mastrigt, R., Coolsaet, B.L., van Duyl, W.A., 1981. First results of stepwise straining of the human urinary bladder and human bladder strips. Invest. Urol. 19 (1), 58–61.

Menzel, R., Böl, M., Siebert, T., 2017. Importance of contraction history on muscle force of porcine urinary bladder smooth muscle. Int. Urol. Nephrol. 49 (2), 205–214.

Morales-Orcajo, E., Siebert, T., Böl, M., 2018. Location-dependent correlation between tissue structure and the mechanical behaviour of the urinary bladder. Acta Biomater. 75, 263–278.

Nagatomi, J., Gloeckner, D.C., Chancellor, M.B., de Groat, W.C., Sacks, M.S., 2004. Changes in the biaxial viscoelastic response of the urinary bladder following spinal cord injury. Ann. Biomed. Eng. 32 (10), 1409–1419.

Nagatomi, J., Toosi, K.K., Chancellor, M.B., Sacks, M.S., 2008. Contribution of the extracellular matrix to the viscoelastic behavior of the urinary bladder wall. Biomech. Model. Mechanobiol. 7 (5), 395–404.

Nagatomi, J., Toosi, K.K., Grashow, J.S., Chancellor, M.B., Sacks, M.S., 2005. Quantification of bladder smooth muscle orientation in normal and spinal cord injured rats. Ann. Biomed. Eng. 33 (8), 1078–1089.

Natali, A.N., Audenino, A.L., Artibani, W., Fontanella, C.G., Carniel, E.L., Zanetti, E.M., 2015. Bladder tissue biomechanical behavior: Experimental tests and constitutive formulation. J. Biomech. 48 (12), 3088–3096.

Natali, A.N., Carniel, E.L., Gregersen, H., 2009. Biomechanical behaviour of oesophageal tissues: Material and structural configuration, experimental data and constitutive analysis. Med. Eng. Phys. 31 (9), 1056–1062.

Nenadic, I.Z., Qiang, B., Urban, M.W., de Araujo Vasconcelo, L.H., Nabavizadeh, A., Alizad, A., Greenleaf, J.F., Fatemi, M., 2013. Ultrasound bladder vibrometry method for measuring viscoelasticity of the bladder wall. Phys. Med. Biol. 58 (8), 2675–2695.

Parekh, A., Cigan, A.D., Wognum, S., Heise, R.L., Chancellor, M.B., Sacks, M.S., 2010. Ex vivo deformations of the urinary bladder wall during whole bladder filling: Contributions of extracellular matrix and smooth muscle. J. Biomech. 43 (9), 1708–1716.

Parsons, B.A., Drake, M.J., Gammie, A., Fry, C.H., Vahabi, B., 2012. The validation of a functional, isolated pig bladder model for physiological experimentation. Front. Pharmacol. (ISSN: 1663-9812) 3, 1–8.

Pel, J.J.M., van Asselt, E., van Mastrigt, R., 2005. Contractile properties of inner and outer smooth muscle bundles from pig urinary detrusor. Urol. Res. 33 (1), 23–30.

Rezakhaniha, R., Agianniotis, A., Schrauwen, J.T., Griffa, A., Sage, D., Bouten, C.V., van de Vosse, F.N., Unser, M., Stergiopulos, N., 2012. Experimental investigation of collagen waviness and orientation in the arterial adventitia using confocal laser scanning microscopy. Biomech. Model. Mechanobiol. 11 (3), 461–473.

Rocha, J.N., 2017. Cystometric analysis of the transplanted bladder. Int. Braz. J. Urol. 43 (1), 112–120.

Rohrmann, D., Zderic, S.A., Duckett, Jr., J.W., Levin, R.M., Damaser, M.S., 1997. Compliance of the obstructed fetal rabbit bladder. Neurourol. Urodyn. 16 (3), 179–189.

Sacks, M.S., Gloeckner, D.C., 1999. Quantification of the fiber architecture and biaxial mechanical behavior of porcine intestinal submucosa. J. Biomed. Mater. Res. 46 (1), 1–10.

Seydewitz, R., Menzel, R., Siebert, T., Böl, M., 2017. Three-dimensional mechano-electrochemical model for smooth muscle contraction of the urinary bladder. J. Mech. Behav. Biomed. Mater. 75 (1), 128–146.

Sommer, G., Haspinger, D.C., Andrä, M., Sacherer, M., Viertler, C., Regitnig, P., Holzapfel, G.A., 2015. Quantification of shear deformations and corresponding stresses in the biaxially tested human myocardium. Ann. Biomed. Eng. 43 (10), 2334–2348.

Sommer, G., Schriefl, A., Zeindlinger, G., Katzensteiner, A., Ainödhofer, H., Saxena, A., Holzapfel, G.A., 2013. Multiaxial mechanical response and constitutive modeling of esophageal tissues: Impact on esophageal tissue engineering. Acta Biomater. 9 (12), 9379–9391.

Takezawa, K., Kondo, M., Kiuchi, H., Soda, T., Takao, T., Miyagawa, Y., Tsujimura, A., Nonomura, N., Shimada, S., 2014. Combination of bladder ultrasonography and novel cystometry method in mice reveals rapid decrease in bladder capacity and compliance in lps-induced cystitis. Am. J. Physiol.-Renal Physiol. 307 (2), f234–241.

Toosi, K.K., Nagatomi, J., Chancellor, M.B., Sacks, M.S., 2008. The effects of long-term spinal cord injury on mechanical properties of the rat urinary bladder. Ann. Biomed. Eng. 36 (9), 1470–1480.

Vaughan, C.W., Satchell, P.M., 1995. Urine storage mechanisms. Prog. Neurobiol. 46 (2), 215–237.

Wall, L.L., Wiskind, A.K., Taylor, P.A., 1994. Simple bladder filling with a cough stress test compared with subtracted cystometry for the diagnosis of urinary incontinence. Am. J. Obstet. Gynecol. 171 (6), 1472–1479.

Wang, C.C., Nagatomi, J., Toosi, K.K., Yoshimura, N., Hsieh, J.H., Chancellor, M.B., Sacks, M.S., 2009. Diabetes-induced alternations in biomechanical properties of urinary bladder wall in rats. Urology 73 (4), 911–915.

Zanetti, E.M., Perrini, M., Bignardi, C., Audenino, A.L., 2012. Bladder tissue passive response to monotonic and cyclic loading. Biorheology 49 (1), 49–63.

Zhao, J., Liao, D., Chen, P., Kunwald, P., Gregersen, H., 2008. Stomach stress and strain depend on location, direction and the layered structure. J. Biomech. 41 (16), 3441–3447.